Available online at www.sciencedirect.com

SciVerse ScienceDirect

Ceramics International 38 (2012) 5713–5722

CERAMICS INTERNATIONAL

www.elsevier.com/locate/ceramint

Structural and dielectrical properties of Mg_3–$Ca_3(PO_4)_2$ bioceramics obtained from hydroxyapatite by sol–gel method

O. Kaygili *, C. Tatar, F. Yakuphanoglu

Department of Physics, Faculty of Science, Firat University, 23119 Elazig, Turkey

Received 18 January 2012; received in revised form 26 March 2012; accepted 4 April 2012
Available online 13 April 2012

Abstract

Mg_3–$Ca_3(PO_4)_2$ bioceramics were prepared from hydroxyapatite (HAp) with high Mg contents using sol–gel method. The influence of magnesium on the phase composition, crystal structure, electrical properties, chemical structure and morphological characteristics of powder bioceramics was analyzed using X-ray diffraction (XRD), Fourier transform infrared (FTIR) spectroscopy and scanning electron microscopy (SEM). Dielectrical properties of the bioceramics were investigated by a dielectric impedance spectroscopy method. It was observed that the crystallization degree for all the samples dramatically was decreased with the increasing Mg content. The average crystallite size of the samples was found to vary from 32 to 42 nm. The morphology, density and dielectric properties of the bioceramics were changed with the addition of the amount of Mg. The obtained results indicate that the Mg_3–$Ca_3(PO_4)_2$ bioceramics can be prepared by means of hydroxyapatite bioceramic.

Keywords: B. Electron microscopy; C. Dielectric properties; Bioceramics; Sol–gel growth

1. Introduction

Among different forms of calcium phosphates, the hydroxyapatite ($Ca_{10}(PO_4)_6(OH)_2$, HAp) is an important bioceramic material, and it is widely used in various clinical applications as an implant material, including bone repair and coatings for metallic implants because of its excellent biocompatibility and bioactivity [1–4]. As it is known that the synthetic HAp is similar in composition to the mineral component of bone and teeth [5,6]. Synthesized HAp has a hexagonal structure with the space group $P6_3/m$, $\alpha = \beta = 90^\circ$, $\gamma = 120^\circ$, and its lattice parameters are $a = b = 0.9418$ nm and $c = 0.6884$ nm [7,8]. Moreover, HAp is a dielectric material, which can be used in electronic systems [9] and the electronic properties of these materials, including microstructure and bonding of HAp ceramics, are very significant for electronic systems. A number of variables, such as preparation methods, Ca/P ratios, nonstoichiometries, defects, size of the nano-crystals and surface reaction with the atmosphere, play a major role for the electronic properties of HAp. Therefore, so as to investigate the electronic structure, it is essential to study the atomic properties of the constituents in HAp material, synthesized by the sol–gel method. There are many HAp preparation techniques such as chemical co-precipitation, spray-pyrolysis and sol–gel [5,10–15]. The preparation technique and the conditions of synthesis are very important parameters for manufacturing process, and they can affect the chemical, structural and morphological properties of HAp. In comparison to the other manufacturing techniques, sol–gel method has many advantages, including high product purity and low synthesis temperature. Furthermore, this method is very useful for the synthesis of nanocrystalline HAp powders [7,16]. Mg is one of the most essential elements in the biological hard tissues, and the effects of the Mg content on many properties (e.g. chemical, physical and microstructure etc.) in calcium phosphate ceramics, such as hydroxyapatite and tricalcium phosphate (TCP), have been investigated by many researchers [17–20].

The aim of present study is to prepare Mg_3–$Ca_3(PO_4)_2$ bioceramics by means of HAp using high Mg contents. The structural and electrical properties of new bioceramic materials were characterized using Fourier transform infrared (FTIR) spectroscopy, X-ray diffraction (XRD), dielectrical impedance spectroscopy and scanning electron microscopy (SEM) techniques.

* Corresponding author. Tel.: +90 424 2370000/3623; fax: +90 424 2330062.
E-mail address: okaygili@firat.edu.tr (O. Kaygili).

0272-8842/$36.00
http://dx.doi.org/10.1016/j.ceramint.2012.04.016

2. Materials and methods

All the bioceramic samples were synthesized by sol–gel technique. All the precursors and their amounts used in this study are given in Table 1. Firstly, calcium nitrate tetra hydrate ($Ca(NO_3)_2{\cdot}4H_2O$) and phosphorus pentoxide (P_2O_5) precursors with Ca/P ratio of 1.67 were used in the preparation process of HAp. These precursors were dissolved in absolute ethanol (C_2H_5OH) by a magnetic stirrer at the ambient temperature for 30 min. Then, this solution was stirred in a vortex for 10 min, and the solution started to transform into a gel. This gel was heated in a hot-water bath at 60 °C for 2 h, and it was dried in an oven at 120 °C for 15 h. Finally, the dried gel was sintered in an electric furnace at 900 °C for 1 h.

The preparation processes of Mg based bioceramic samples were similar to the preparation process of HAp. The only difference was the addition of magnesium nitrate hexahydrate ($Mg(NO_3)_2{\cdot}6H_2O$), which was dissolved in absolute ethanol, in the solutions of the calcium nitrate tetrahydrate and phosphorus pentoxide. The other processes, containing the stirring, drying and heating stages were similar to the preparation of the HAp.

All the FTIR measurements of the bioceramic samples were carried out using a PerkinElmer Spectrum One spectrophotometer in the region of 400–4000 cm^{-1} using the KBr pellet technique with a spectral resolution of 4 cm^{-1}. X-ray diffraction (XRD) measurements of the bioceramic samples were recorded with a Bruker D8 Advance Diffractometer with CuKα (λ = 0.15406 nm) radiation at a step of 0.02°/s in the range of 15–70°. The measurements of the electrical resistances of all the samples were performed using a KEITHLEY 6517A electrometer. The dielectrical parameters of the samples were measured using a HIOKI 3532-50 LCR HiTESTER at frequencies between 42 Hz and 5 MHz at room temperature. The density values of the samples were calculated with Archimedes method. The samples were uniaxially compacted using a steel mold with an internal diameter of 13 mm at a pressure of 100 MPa. For scanning electron microscope (SEM) measurements, the samples were coated with gold. Then, the observing and analyzing procedures of the microstructures of the gold coated samples were performed by a JEOL JSM 7001F scanning electron microscope (SEM) combined with an X-ray energy dispersive spectrometer (EDS) at an accelerating voltage of 20 kV.

Table 1
Chemical compositions of the bioceramic samples.

Sample	$Ca(NO_3)_2{\cdot}4H_2O$ (mol)	P_2O_5 (mol)	$Mg(NO_3)_2{\cdot}6H_2O$ (mol)
HAp	0.050	0.015	–
MG1	0.040	0.015	0.010
MG2	0.030	0.015	0.020
MG3	0.025	0.015	0.025
MG4	0.020	0.015	0.030
MG5	0.010	0.015	0.040

3. Results and discussion

The structural properties of the samples were analyzed by FTIR spectra, and Fig. 1 displays the FTIR spectra of the bioceramic samples. As seen in Fig. 1, the FTIR spectra of the HAp give the intensive bands originating from vibrations of PO_4^{3-} groups. The characteristics absorption bands of the HAp are at 603 and at 570 cm^{-1}. These bands are attributed to the bending vibrations of P–O groups. The most intensive bands at 1043 and 1091 cm^{-1} corresponds to triply degenerate antisymmetric vibrations of the P–O bands. The peak assigned to the libration band of the hydroxyl group was obtained, except for MG5 sample, and the peak assigned to the characteristic stretching band of the hydroxyl group disappeared after high Mg content. Instead of this peak, the broad bands originated from the presence of adsorbed water were observed in the region around 3300–3600 cm^{-1} [21]. Furthermore, the other broad bands at 1630 cm^{-1} were found for all the samples. As given in Table 2, the bands belonging to the internal modes (υ_4, υ_3 and υ_1) of the phosphate groups were seen in FTIR spectra of the samples [22,23]. The bands at 1382 cm^{-1} attributed to residual nitrate groups were observed for all the samples. These bands were probably originated from the synthesis precursors such as calcium nitrate and/or magnesium nitrate [24]. The sharp peaks belonging to the

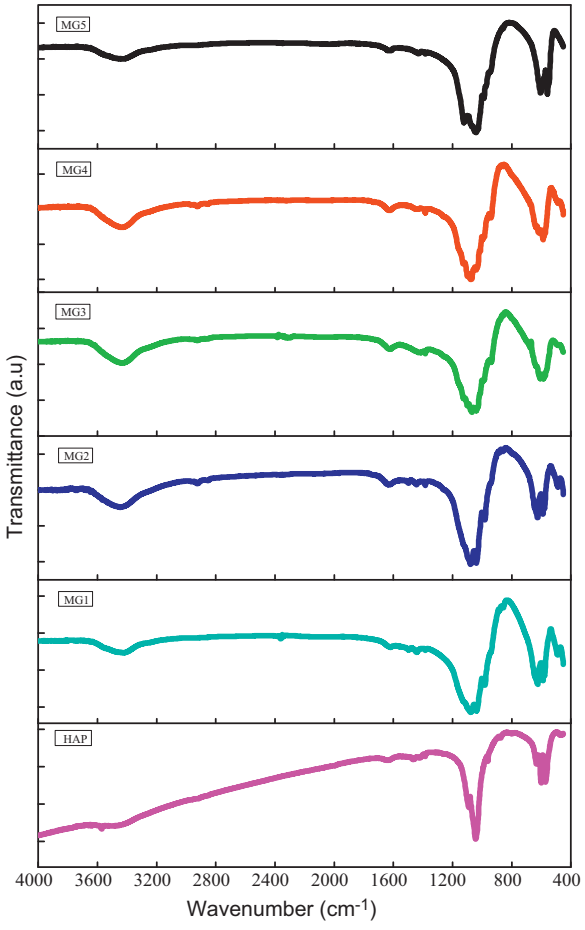

Fig. 1. FTIR results of the samples.

Table 2
The revealed bands and their assignments for FTIR spectra measurements of all the samples.

Peak (cm^{-1})						
HAp	MG1	MG2	MG3	MG4	MG5	Assignment
631	623	625	633	633	–	Libration mode of the hydroxyl group
3571	–	–	–	–	–	Stretching mode of the hydroxyl group
570, 601	488, 577, 588	485, 576, 589	491, 586, 606, 672	488, 587, 609	558, 604	Stretching mode (υ_4) of the O–P–O bonds of phosphate group
1045, 1088	980, 993, 1039, 1072	979, 1034, 1078	990, 1039, 1070, 1097, 1119	995, 1039, 1072, 1097, 1119	987, 1039, 1067, 1122	Asymmetric stretching mode (υ_3) of the P–O bonds of phosphate group
960	946	–	941	938	946	Symmetric stretching mode (υ_1) of the P–O bonds of phosphate group
1637	1615, 1640, 3421	1624, 3445	1620, 3435	1627, 3434	1616, 1637, 3429	Vibration mode of the adsorbed water
	1495	1496	–	–	–	Characteristic stretching mode (υ_3) of the carbonate group
1467	–	–	–	–	–	Characteristic stretching mode (υ_1) of the carbonate group in A-type
1421	1440	1443	1427	1432	1432	Stretching mode (υ_1) of the carbonate group in B-type
872	880	877	876	–	–	Bending mode (υ_4 or υ_3) of the carbonate group
–	856	856	859	853	858	Stretching mode (υ_3) of the carbonate group
–			2287–2400			Band gap of the atmospheric carbon dioxide
			2856, 2926			Stretching mode of the C–H bonds
			1382			The N–O stretch of the nitrate group

hydroxyl and phosphate groups in FTIR spectrum of HAp sample confirm the well-crystallized apatite structure, and support the XRD results [25]. In comparison to HAp sample, the sharpness of these peaks for Mg-doped samples decreases. In addition, the bands corresponding to the stretching and bending modes of the carbonate group were obtained, and the carbonate ions are a common impurity for hydroxyapatite structure [21,26–28]. These ions cause the defects in the structure, because they are substituted with the hydroxyl groups for A-type or the phosphate for B-type. Both substitutions affect the lattice parameters of the apatite structure [29].

As seen in Fig. 2, the agglomerated structures were observed in SEM images of all the bioceramic samples. The ratio of Ca/P for the HAp sample was found to be 1.61 and it is closer to the 1.67 value. The ratio of (Ca + Mg)/P was changed with the addition of Mg. This indicates that the Mg is substituted into HAp and this substitution leads to a crystal defect. Therefore, the ratio of (Ca + Mg)/P for the ceramics were changed. Effect of Mg content on microstructure is not observable due to the too much agglomeration, because this agglomeration does not allow distinguishing of the microstructure change.

XRD patterns of the bioceramic samples with various molar fractions of Mg are shown in Fig. 3. The lattice parameters of the HAp was determined using a relation between miller indices, lattice parameters and interplane distance [30] and are given in Table 3, and the values of d, 2θ and Miller indices belonging to HAp sample are listed and compared to the JCPDS (Joint Committee on Powder Diffraction Standards) data (PDF 09-432) in Table 4. As can be seen in Tables 3 and 4, there is a good agreement between the unit cell parameters of the standard values of hydroxyapatite and the parameters calculated from XRD patterns. Two minor peaks belonging to the β-TCP (PDF 09-169) structure were obtained. The hexagonal structure of the HAp sample transforms into the other crystal systems, including monoclinic and rhombohedral. With the increase of the molar ratio of Mg, the new calcium-magnesium phosphate phases, containing Stanfieldite $Mg_3Ca_3(PO_4)_4$ (PDF 73-1182), $Ca_{2.86}Mg_{0.14}(PO_4)_2$ (PDF 70-681), $(Ca_{2.589}Mg_{0.411})(PO_4)_2$ (PDF 87-1582) and $(Ca,Mg)_3(PO_4)_2$ (PDF 13-404), are formed in the doped samples. On the other hand, HAp and β-TCP phases disappear with the addition of Mg.

In addition, the average crystallite size (D) for the samples was calculated by using Scherrer equation:

$$D = \frac{k\lambda}{B_{1/2}\cos\theta} \quad (1)$$

where k is the constant equal to 0.9, and $B_{1/2}$ is the full width at half maximum (FWHM) of X-ray reflection in the radian [30,31].

The crystallization degree of the HAp changes with Mg dopant. The crystallization degree (X_C) of the samples can be calculated from the following relation:

$$X_C \approx 1 - \frac{V_{112/300}}{I_{300}} \quad (2)$$

where $V_{1\,1\,2/3\,0\,0}$ is the intensity of the hollow between (1 1 2) and (3 0 0) reflections, and $I_{3\,0\,0}$ is the intensity of the reflection

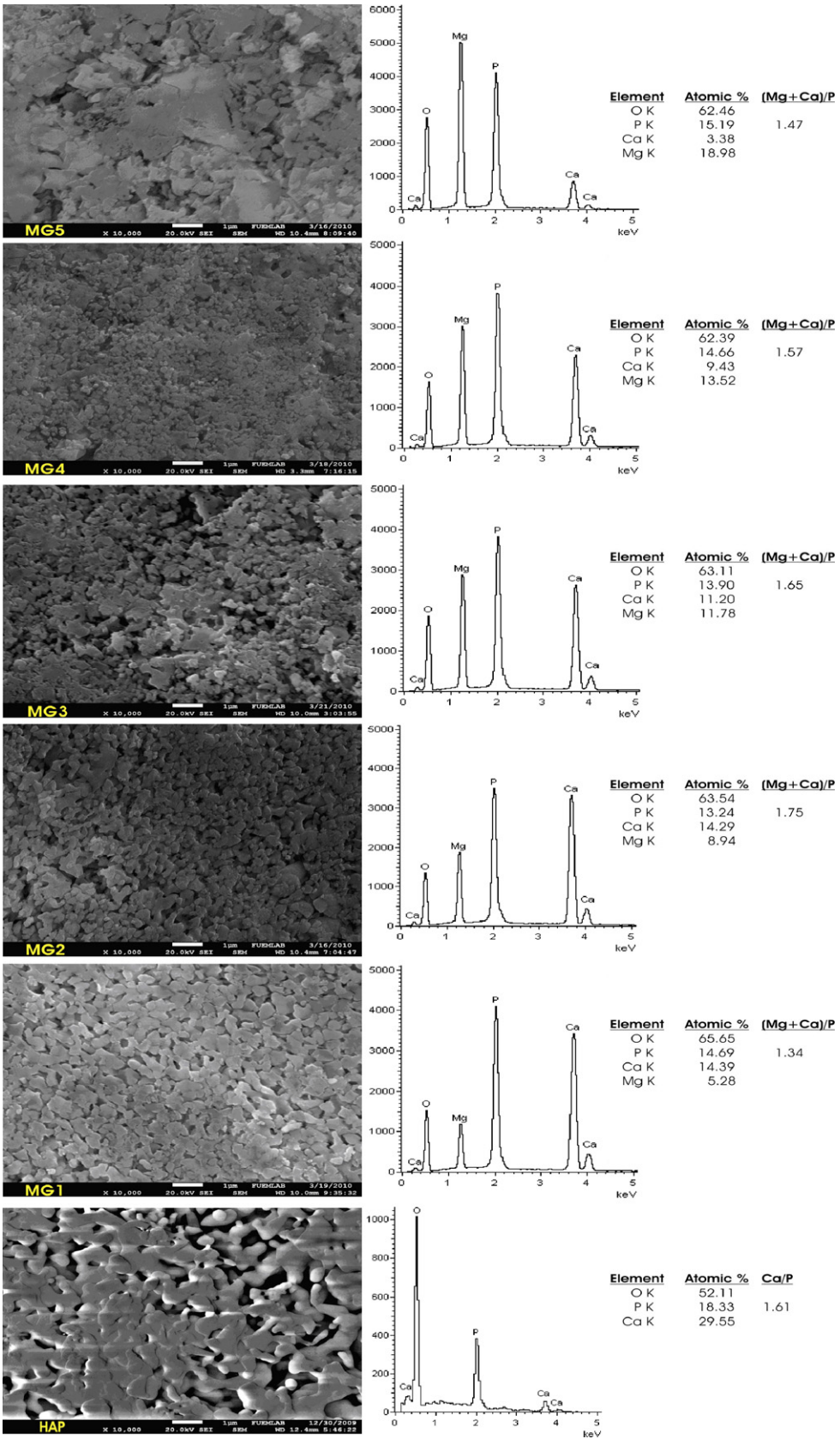

Fig. 2. SEM micrographs and EDX analysis results of all the bioceramic samples.

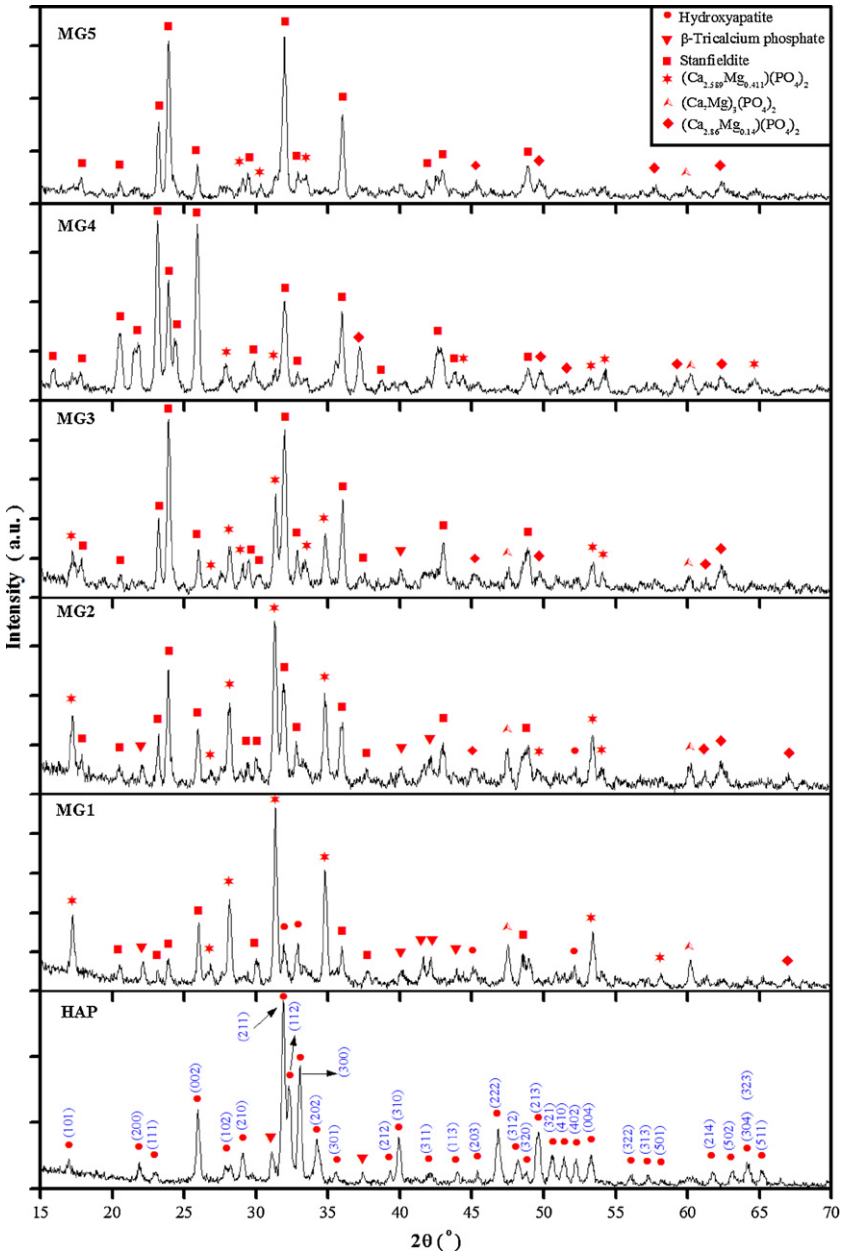

Fig. 3. XRD patterns of the samples.

belonging to (3 0 0) plane [31]. The degree of the crystallization and the average crystallite sizes of all the samples are given in Table 5. The degree of crystallization of the samples dramatically decreases with the molar percentage of Mg, and this result is in the agreement with Bigi et al. [32]. The average crystallite sizes of all the samples are in the range from 30 to 42 nm. This suggests that all the samples are the nanostructured materials [33].

Electrical resistances of these samples were measured at 200 V dc, and the values of the resistance of all the samples are listed in Table 6. The resistance values are about 10^{11} Ω. As expected, all the bioceramic samples exhibit the insulator behavior [34].

The plots of the dielectric impedance parameters, including the impedance (Z), capacitance (C_p), ac conductivity (σ_{ac}), dielectric constant (ε') and dielectric loss (ε''), versus frequency are shown in Figs. 4–8, respectively.

Table 3
The lattice parameters, *c*/*a* ratio and volume of the unit cell of HAp sample.

Sample	*a* (nm)	*c* (nm)	*c*/*a*	*V* (nm)^3	% *a*	% *c*	% *c*/*a*	% *V*
HAp (JCPDS 09-432)	0.9418	0.6884	0.73094	0.52878	0	0	0	0
HAp	0.9402	0.6879	0.73165	0.52660	−0.17	−0.07	0.10	−0.41

Table 4
d, 2θ and Miller indices values for the reference sample.

Peak number	Observed values		Calculated values		Miller indices		
	d (nm)	2θ	d (nm)	2θ	h	k	l
1	0.5230	16.94	0.5261	16.84	1	0	1
2	0.4103	21.64	0.4078	21.78	2	0	0
3	0.3864	23.00	0.3887	22.86	1	1	1
4	0.3432	25.94	0.3442	25.86	0	0	2
5	0.3160	28.22	0.3171	28.12	1	0	2
6	0.3070	29.06	0.3083	28.94	2	1	0
7	0.2815	31.76	0.2814	31.78	2	1	1
8	0.2783	32.14	0.2779	32.19	1	1	2
9	0.2710	33.03	0.2719	32.92	3	0	0
10	0.2292	39.28	0.2296	39.20	2	1	2
11	0.2262	39.82	0.2262	39.82	3	1	0
12	0.2218	40.64	0.2228	40.46	2	2	1
13	0.2140	42.20	0.2149	42.01	3	1	1
14	0.2059	43.94	0.2063	43.85	1	1	3
15	0.1996	45.40	0.2000	45.31	2	0	3
16	0.1942	46.73	0.1943	46.70	2	2	2
17	0.1887	48.20	0.1890	48.09	3	1	2
18	0.1870	48.66	0.1871	48.62	3	2	0
19	0.1840	49.50	0.1841	49.48	2	1	3
20	0.1805	50.54	0.1806	50.50	3	2	1
21	0.1778	51.36	0.1780	51.29	4	1	0
22	0.1753	52.14	0.1754	52.09	4	0	2
23	0.1716	53.34	0.1721	53.18	0	0	4
24	0.1686	54.36	0.1644	55.88	3	2	2
25	0.1612	57.08	0.1611	57.13	3	1	3
26	0.1587	58.14	0.1587	58.12	5	0	1
27	0.1501	61.74	0.1503	61.68	2	1	4
28	0.1471	63.15	0.1474	63.01	5	0	2
29	0.1452	64.10	0.1454	63.97	3	0	4
30	0.1448	64.26	0.1450	64.17	3	2	3
31	0.1431	65.14	0.1433	65.04	5	1	1

Table 5
The calculated values of crystallite sizes and degree of crystallization from XRD peaks.

Sample	D (nm)	X_C
HAp	33.74	0.90
MG1	33.48	0.89
MG2	38.74	0.73
MG3	42.00	0.64
MG4	30.01	0.51
MG5	38.61	0.46

Table 6
The electrical resistance values of the samples.

Sample	R (Ω)
HAp	1.27×10^{11}
MG1	1.25×10^{11}
MG2	6.00×10^{11}
MG3	2.40×10^{11}
MG4	1.60×10^{11}
MG5	1.82×10^{11}

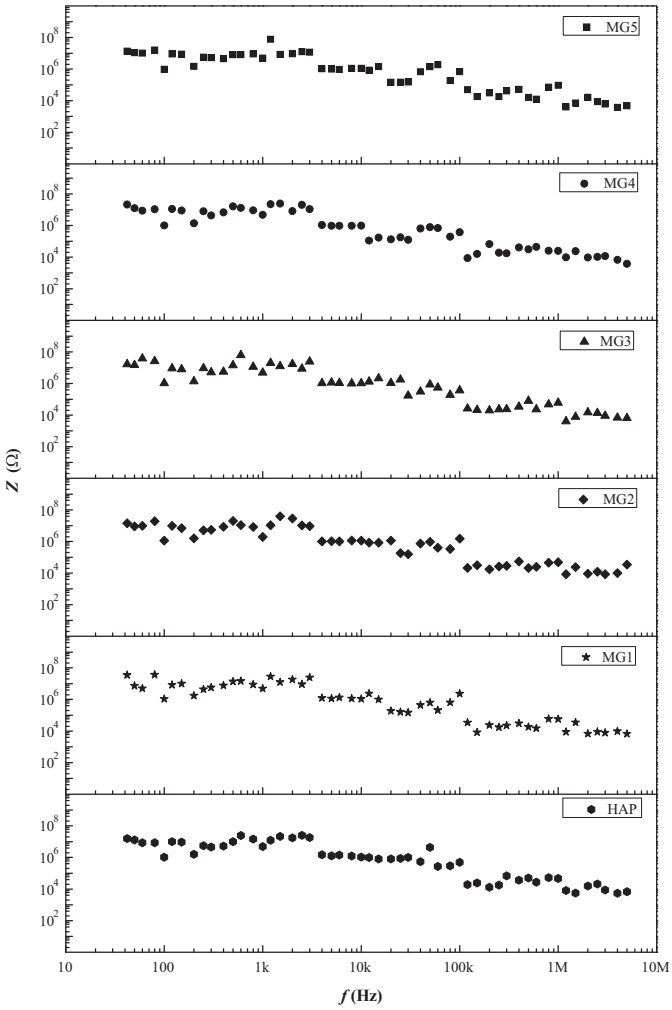

Fig. 4. The plots of impedance (Z) versus frequency (f) for all the samples.

The alternating current conductivity dependence of frequency can be expressed by the following relation [35]:

$$\sigma_{ac} = \sigma_{dc} + B\omega^s \quad (3)$$

where σ_{dc} is the direct current conductivity, B is a constant, ω is the angular frequency and s is an exponent. The ac conductivity mechanism was analyzed by Eq. (3) and s value was plotted as a function of concentration of Mg dopant. Fig. 9 shows the plot of s versus concentration of Mg. As seen in Fig. 6, the ac conductivity for all the investigated samples increases almost linearly with increasing frequency. This suggests that the frequency of the applied field is lower than the charge carrier jump frequency in the solid [36]. The s value changes with the increase of Mg dopant. This behavior can be attributed to the interaction between HAp and Mg ion influencing the AC transport phenomenon, because the s value is the characteristic parameter representing many body interactions of the electrons, charges and impurities. The ac conductivity mechanism of the bioceramic samples obeys with the power law dependence of ac conductivity on frequency. This law corresponds to the short range hopping of charge carriers through trap sites that are separated by energy barriers of varied heights [37].

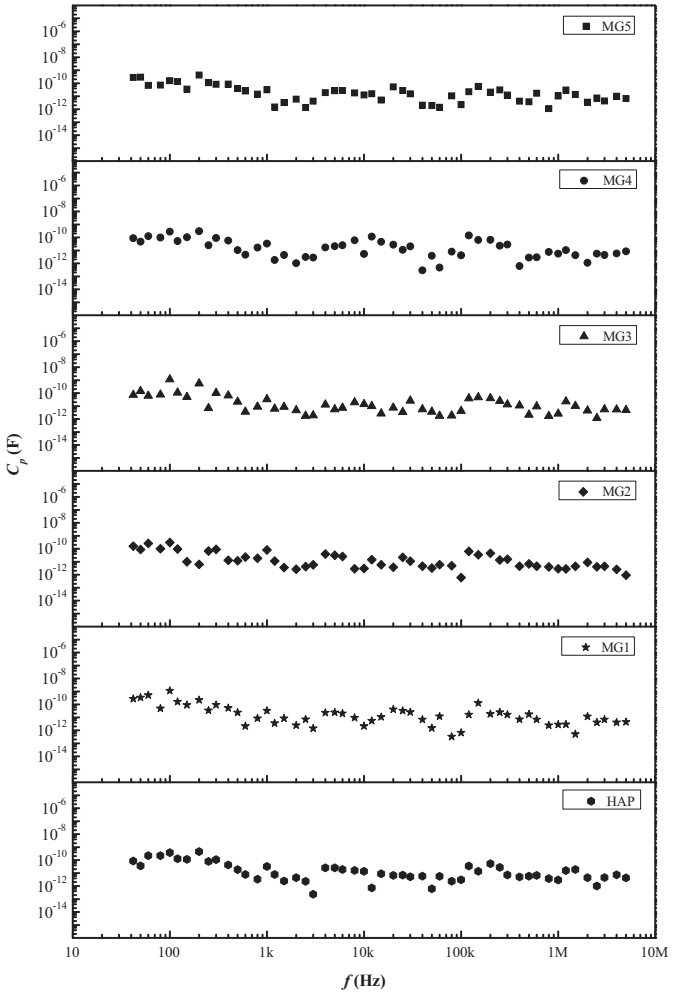

Fig. 5. The plots of capacitance (C_p) versus frequency (f) for all the samples.

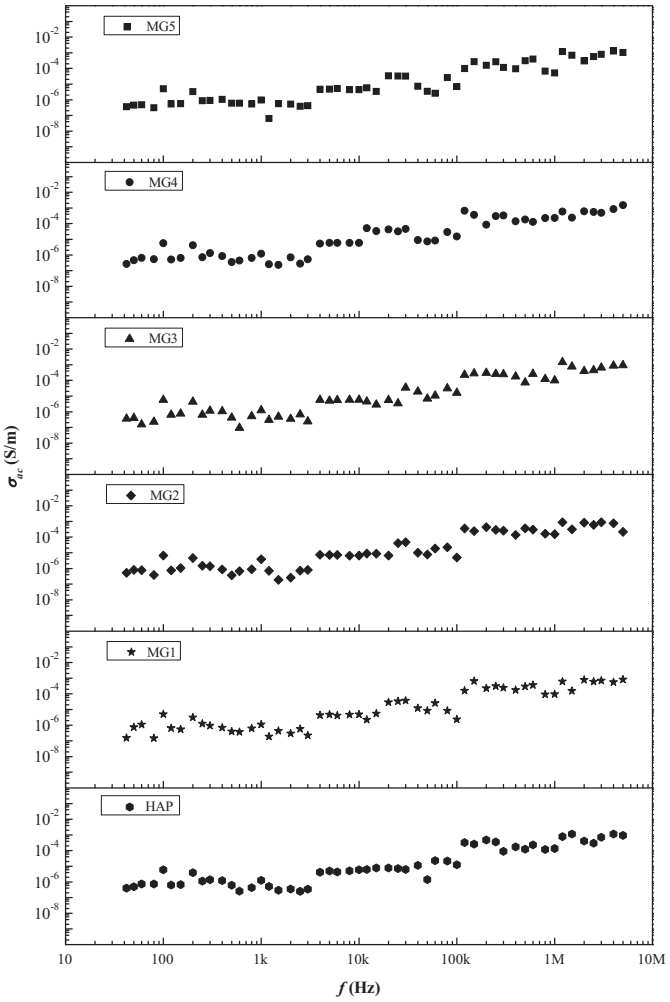

Fig. 6. The plots of ac conductivity (σ_{ac}) versus frequency (f) for all the samples.

The values of the dielectric constant were determined by the following equation:

$$\varepsilon' = \frac{C_p \times t}{\varepsilon_o A} \tag{4}$$

where t is the thickness of the sample, ε_o is the permittivity of the vacuum and A is the area of cross-section of the sample [38]. The dielectric constants of all the bioceramic samples at the different frequencies were given in Table 7. The impedance and capacitance values decrease with frequency, but the values of the ac conductivity increase. As seen in Fig. 7, the value of dielectric constant changes with the increase of frequency values in the range of 42 Hz and 5 MHz [39]. The dielectric constant of the samples has some fluctuations. These fluctuations can be low dielectrical polarization ability of the samples with Mg content.

The densities of the samples can be calculated by Archimedes method [40]

$$\rho = \frac{W_a}{W_a - W_b}\rho_\ell \tag{5}$$

Table 7
The dielectric constant values of the samples for different frequencies.

Sample	Dielectric constant (ε')						
	$\varepsilon'_{500\,\mathrm{Hz}}$	$\varepsilon'_{1\,\mathrm{kHz}}$	$\varepsilon'_{5\,\mathrm{kHz}}$	$\varepsilon'_{10\,\mathrm{kHz}}$	$\varepsilon'_{200\,\mathrm{kHz}}$	$\varepsilon'_{500\,\mathrm{kHz}}$	$\varepsilon'_{1\,\mathrm{MHz}}$
HAp	13.04	22.91	17.91	9.52	37.15	4.09	2.06
MG1	14.20	19.70	14.28	1.29	11.00	10.45	1.67
MG2	10.07	68.19	26.22	2.57	37.98	5.70	2.44
MG3	14.65	22.17	3.78	9.34	26.81	1.44	1.71
MG4	6.83	21.73	16.66	3.48	41.83	1.93	3.69
MG5	21.60	17.39	14.79	6.92	11.30	2.09	5.70

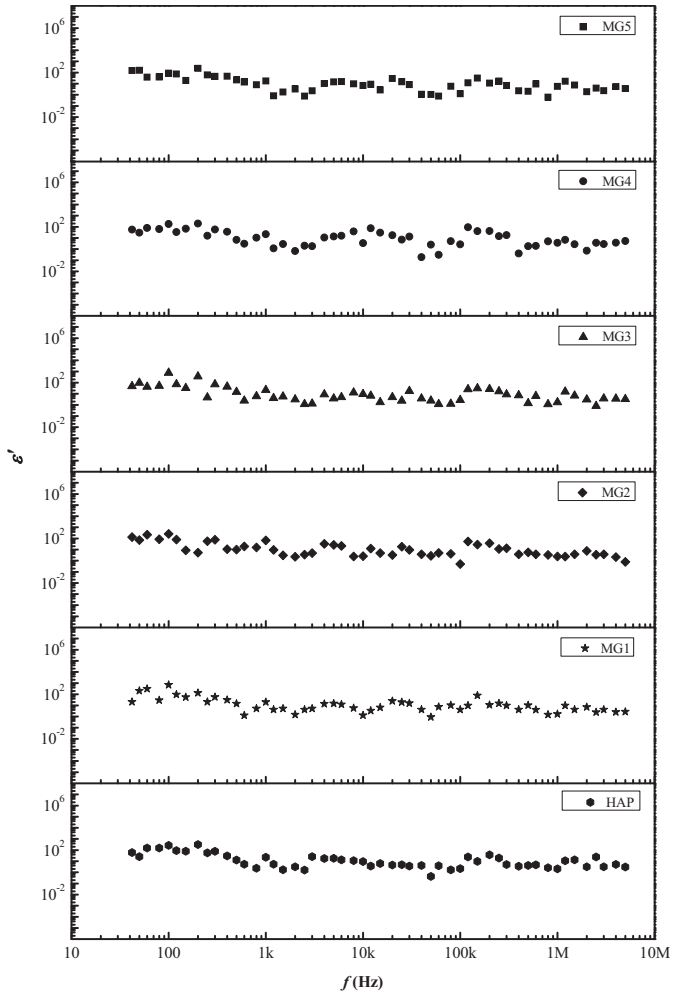

Fig. 7. The plots of dielectric constant (ε') versus frequency (f) for all the samples.

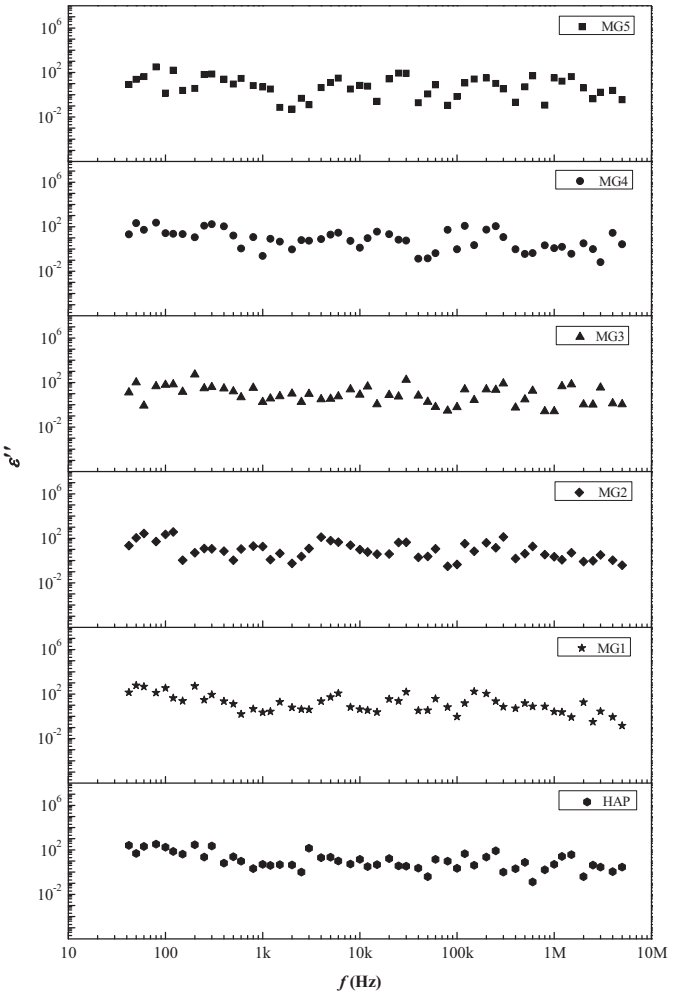

Fig. 8. The plots of dielectric loss (ε'') versus frequency (f) for all the samples.

where ρ is the density of the solid sample and ρ_ℓ is the density of the immersion liquid. Also, W_a and W_b are weights of the sample in air and liquid, respectively. The obtained density values of the samples are given in Table 8. The density of the HAp was calculated to be 2.74 g cm^{-3}, and this value is smaller than that of the theoretical density of the hydroxyapatite. However, this value is very close to the density of the commercial HAp (2.70 g cm^{-3}) [41]. Densities of the Mg-doped samples were calculated to be 2.50, 2.38, 2.32, 2.20 and 2.01 g cm^{-3} for MG1, MG2, MG3, MG4 and MG5 samples, respectively. The density values of the samples decrease with the increase of the molar ratio of Mg. The obtained ρ values of the studied bioceramics are lower than the Mg-substituted hydroxyapatite samples. The decrease in ρ values of the samples can depend on the ionic substitutions in the apatite structure causing the structural defects [42].

Table 8
The densities of the samples calculated from Archimedes principle.

Sample	ρ (g cm^{-3})
HAp	2.74
MG1	2.50
MG2	2.38
MG3	2.32
MG4	2.20
MG5	2.01

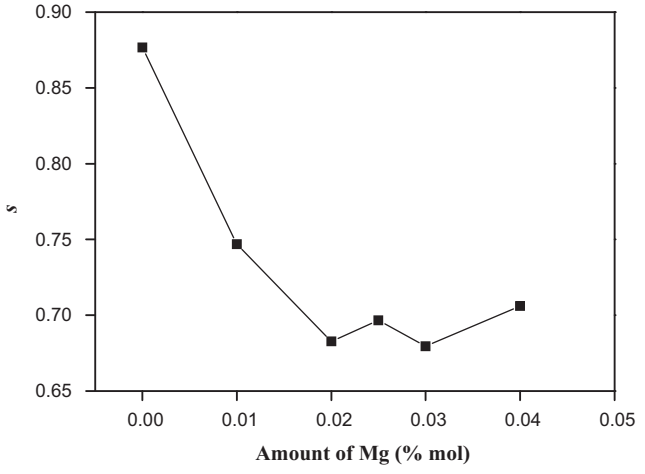

Fig. 9. Variation of the angular frequency exponent (s) versus the amount of Mg.

4. Conclusions

Mg-doped hydroxyapatite bioceramic samples were perfectly prepared by sol–gel method. Many properties of hydroxyapatite, including electrical, microstructure, chemical and physical, changed by Mg-addition. From the XRD patterns, the hydroxyapatite was the major phase, and β-TCP was the minor phase for HAp sample. In comparison to HAp sample, the new phases based on magnesium–calcium phosphates appeared, and hydroxyapatite and β-TCP phases gradually disappeared with the addition of Mg. Moreover, the crystal structures changed with the molar ratio of Mg dopant. With regard to the electrical properties, all the samples exhibited the insulator behavior, because of their high electrical resistances of 10^{11} Ω. It was observed that many changes occurred in the values of dielectric constant, capacitance and ac conductivity of all the samples depending on the increasing frequency value. Moreover, impedance values of all the samples were high for low frequency values, yet with the increase of frequency values, the impedance values underwent an obvious decrease. The density values of Mg-doped samples dramatically decreased with the molar ratio of Mg dopant. FTIR spectrum of HAp sample was perfectly in agreement with original hydroxyapatite structure. All the samples predominantly had phosphate and hydroxyl groups, and phosphate peaks in FTIR spectra supported the phosphate based phases obtained by XRD analysis.

It is evaluated that Mg_3–$Ca_3(PO_4)_2$ bioceramics can be obtained from hydroxyapatite with high Mg contents.

Acknowledgement

This work was supported by Management Unit of Scientific Research projects of Firat University (FÜBAP) (Project Number: 1676).

References

[1] T. Yamamuro, L.L. Hench, J. Wilson, Handbook of Bioactive Ceramics: Volume II. Calcium Phosphate and Hydroxylapatite Ceramics, CRC Press, Boca Raton, 2000.
[2] J. Park, Bioceramics: Properties, Characterizations, and Applications, Springer, New York, 2008.
[3] D. Shi, Introduction to Biomaterials, Tsinghua University Press and World Scientific Publishing Co. Pte. Ltd., Beijing, 2006.
[4] C.B. Carter, M.G. Norton, Ceramic Materials: Science and Engineering, Springer, New York, 2007.
[5] T.S.B. Narasaraju, D.E. Phebe, Some physico-chemical aspects of hydroxylapatite, Journal of Materials Science 31 (1996) 1–21.
[6] H.E. Hosseini, M.R. Houssaindokth, M. Chahkandi, Effects of parameters of sol–gel process on the phase evolution of sol–gel-derived hydroxyapatite, Materials Chemistry and Physics 106 (2007) 310–316.
[7] S.J. Kalita, A. Bhardwaj, H.A. Bhatt, Nanocrystalline calcium phosphate ceramics in biomedical engineering, Materials Science and Engineering C 27 (2007) 441–449.
[8] S.C. Liou, S.Y. Chen, H.Y. Lee, J.S. Bow, Structural characterization of nano-sized calcium deficient apatite powders, Biomaterials 25 (2004) 189–196.
[9] S.J. Reyes-Gasga, R. García-García, M.J. Arellano-Jiménez, E. Sanchez-Pastenes, G.E. Tiznado-Orozco, I.M. Gil-Chavarria, G. Gómez-Gasga, Structural and thermal behaviour of human tooth and three synthetic hydroxyapatites from 20 to 600 °C, Journal of Physics D: Applied Physics 41 (2008) 1–11.
[10] P. Kanchana, C. Sekar, Influence of sodium fluoride on the synthesis of hydroxyapatite by gel method, Journal of Crystal Growth 312 (2010) 808–816.
[11] D.M. Liu, T. Trocznski, W.J. Tseng, Water-based sol–gel synthesis of hydroxyapatite: process development, Biomaterials 22 (2001) 1721–1730.
[12] S. Pramanik, A.K. Agarwal, K.N. Rai, A. Garg, Development of high strength hydroxyapatite by solid-state-sintering process, Ceramics International 33 (2007) 419–426.
[13] M.P. Mahabole, R.C. Aiyer, C.V. Ramakrishna, B. Sreedhar, R.S. Khairnar, Synthesis, characterization and gas sensing property of hydroxyapatite, Bulletin of Materials Science 28 (2005) 535–545.
[14] Y.M. Sung, J.C. Lee, J.W. Yang, Crystallization and sintering characteristics of chemically precipitated hydroxyapatite nanopowder, Journal of Crystal Growth 262 (2004) 467–472.
[15] S.K. Padmanabhan, A. Balakrishnan, M.C. Chu, Y.J. Lee, T.N. Kim, S.J. Cho, Sol–gel synthesis and characterization of hydroxyapatite nanorods, Particuology 7 (2009) 466–470.
[16] D.M. Liu, Q. Yang, T. Trocznski, W.J. Tseng, Structural evolution of sol–gel-derived hydroxyapatite, Biomaterials 23 (2002) 1679–1687.
[17] X. Li, A. Ito, Y. Sogo, X. Wang, R.Z. LeGeros, Solubility of Mg-containing β-tricalcium phosphate at 25 °C, Acta Biomaterialia 5 (2009) 508–517.
[18] J. Marchi, A.C.S. Dantas, P. Greil, J.C. Bressiani, A.H.A. Bressiani, F.A. Müller, Influence of Mg-substitution on the physicochemical properties of calcium phosphate powders, Materials Research Bulletin 42 (2007) 1040–1050.
[19] I. Mayer, R. Scblam, J.D.B. Featberstone, Magnesium-containing carbonate apatites, Journal of Inorganic Biochemistry 66 (1997) 1–6.
[20] J. Kolmas, A. Jaklewicz, A. Zima, M. Bućko, Z. Paszkiewicz, J. Lis, A. Ślósarczyk, W. Kolodziejski, Incorporation of carbonate and magnesium ions into synthetic hydroxyapatite: the effect on physicochemical properties, Journal of Molecular Structure 987 (2011) 40–50.
[21] S. Koutsopoulos, Synthesis and characterization of hydroxyapatite crystals: a review study on the analytical methods, Journal of Biomedical Materials Research 62 (2002) 600–612.
[22] S. Pezzatini, R. Solito, L. Morbidelli, S. Lamponi, E. Boanini, A. Bigi, M. Ziche, The effect of hydroxyapatite nanocrystals on microvascular endothelial cell viability and functions, Journal of Biomedical Materials Research Part A 76 (2005) 656–663.
[23] D.S. Seo, J.K. Lee, Dissolution of human teeth-derived hydroxyapatite, Annals of Biomedical Engineering 36 (2008) 132–140.
[24] D.K. Pattanayak, R. Dash, R.C. Prasad, B.T. Rao, T.R. Mohan, Synthesis and sintered properties evaluation of calcium phosphate ceramics, Materials Science and Engineering C 27 (2007) 684–690.
[25] H. Arami, M. Mohajerani, M. Mazloumi, R. Khalifehzadeh, A. Lak, S.K. Sadrnezhaad, Rapid formation of hydroxyapatite nanostrips via microwave irradiation, Journal of Alloys and Compounds 469 (2009) 391–394.
[26] R.N. Panda, M.F. Hsieh, R.J. Chung, T.S. Chin, FTIR, XRD, SEM and solid state NMR investigations of carbonate-containing hydroxyapatite nano-particles synthesized by hydroxide-gel technique, Journal of Physics and Chemistry of Solids 64 (2003) 193–199.
[27] M. Markovic, B.O. Fowler, M.S. Tung, Preparation and comprehensive characterization of a calcium hydroxyapatite reference material, Journal of Research of the National Institute of Standards and Technology 109 (2004) 553–568.
[28] M. Jevtić, M. Mitrić, S. Škapin, B. Jančar, N. Ignjatović, D. Uskoković, Crystal structure of hydroxyapatite nanorods synthesized by sonochemical homogeneous precipitation, Crystal Growth and Design 8 (2008) 2217–2222.
[29] S. Peroos, Z. Du, N.H. de Leeuw, A computer modelling study of the uptake and distribution of carbonate defects in hydroxy-apatite, Biomaterials 27 (2006) 2150–2161.
[30] B.D. Cullity, Elements of X-ray Diffraction, Addison-Wesley Publishing Company, Massachusetts, 1978.

[31] Z.Y. Li, W.M. Lam, C. Yang, B. Xu, G.X. Ni, S.A. Abbah, K.M.C. Cheung, K.D.K. Luk, W.W. Lu, Chemical composition, crystal size and lattice structural changes after incorporation of strontium into biomimetic apatite, Biomaterials 28 (2007) 1452–1460.

[32] A. Bigi, G. Falini, E. Foresti, M. Gazzano, A. Ripamonti, N. Roveri, Magnesium influence on hydroxyapatite crystallization, Journal of Inorganic Biochemistry 49 (1993) 69–78.

[33] D. Williams, The relationship between biomaterials and nanotechnology, Biomaterials 29 (2008) 1737–1738.

[34] T.T. Davis, A., Vatave, J., Patla, J., Bernbeck, B.R., Delamarter, H.W. Bae, Pedicle Screw Electrical Resistance: Hydroxyapatite Coated versus Non–Coated. American Association of Neurological Surgeons, Orlando, FL, USA, February 17–20, 2010.

[35] F. Yakuphanoglu, F. Senkal, Electrical transport properties of an organic semiconductor on polyaniline doped by boric acid, Polymers for Advanced Technologies 19 (2008) 1876–1881.

[36] J.C. Dyre, The random free-energy barrier model for ac conduction in disordered solids, Journal of Applied Physics 64 (1988) 2456.

[37] S.R. Elliott, A theory of a.c. conduction in chalcogenide glasses, Philosophical Magazine 36 (1977) 1291.

[38] F. Yakuphanoglu, Y.T. Yoo, M. Okutan, An impedance spectroscopy study in poly(butylene adipate) ionomers, Annals of Physics 13 (2004) 559–568.

[39] T.P. Hoepfner, E.D. Case, The porosity dependence of the dielectric constant for sintered hydroxyapatite, Journal of Biomedical Materials Research Part A 60 (2002) 643–650.

[40] O. Kaygili, H. Yavuz, The effects of gamma irradiation on non-isothermal crystallization kinetics and microhardness of the Li_2O–Al_2O_3–SiO_2 glass–ceramic, Journal of Thermal Analysis and Calorimetry 102 (2010) 681–684.

[41] M.A. Fanovich, M.S. Castro, J.M. Porto López, Analysis of the microstructural evolution in hydroxyapatite ceramics by electrical characterisation, Ceramics International 25 (1999) 517–522.

[42] E. Landi, G. Logroscino, L. Proietti, A. Tampieri, M. Sandri, S. Sprio, Biomimetic Mg-substituted hydroxyapatite: from synthesis to in vivo behaviour, Journal of Materials Science: Materials in Medicine 19 (2008) 239–247.